PERGAMON

International Journal of Heat and Mass Transfer 45 (2002) 125–144

International Journal of HEAT and MASS TRANSFER

www.elsevier.com/locate/ijhmt

Magnetic field effects on *g*-jitter induced flow and solute transport

Bo Pan [a], D-Y Shang [a], B.Q. Li [a,*], H.C. de Groh [b]

[a] *School of Management and Materials Engineering, Washington State University, P.O. Box 642920, Pullman, WA 99164-2920, USA*
[b] *NASA Lewis Research Center, Cleveland, OH 44135, USA*

Received 15 November 2000; received in revised form 27 February 2001

Abstract

Numerical modeling and analyses are presented of magnetic damping of *g*-jitter driven fluid flow and its effect on the solutal striation in a simplified Bridgman–Stockbarger crystal growth system under microgravity. The model development is based on the finite element solution of the momentum, energy and solute transport equations under *g*-jitter conditions in the presence of an external magnetic field. The numerical model is verified by comparison with analytical solutions obtained for a simple parallel plate channel flow driven by *g*-jitter in a transverse magnetic field. Simulations are carried out to study the behavior of convective flow and solutal transport induced by the combined *g*-jitter and magnetohydrodynamic forces. Both the idealized single frequency *g*-jitter force and the real *g*-jitter perturbation taken during space flight are considered. Results indicate that an applied magnetic field can effectively damp the velocity caused by *g*-jitter and help to reduce the time variation of solute redistribution. A stronger applied field is more effective in suppressing the convective flows and hence reducing concentration variation. It is found that *g*-jitter driven flows have the same oscillation period as the driving force with or without the applied field. However, an applied magnetic field shortens the transient period over which the flow field evolves into a quasi-steady state time harmonic oscillation after *g*-jitter sets in. The flow intensity increases with an increase in *g*-jitter magnitude but decreases with an increase in the applied field strength. The reduced convection in the liquid pool by the applied magnetic field results in a reduction of the concentration oscillation. The magnetic field is very useful in suppressing the spiking velocities that are induced by the spikes in the real *g*-jitter data. The damping effect is more pronounced if the magnetic field is switched on before the onset of *g*-jitter disturbances.

1. Introduction

Natural convection in the melt pool from which single crystals are grown arises from the combined action of temperature gradients in the melt and the earth gravity. The convective flows can have a profound effect on the solute distribution in the liquid and thus have important implications for the solute uniformity and defects formation in the crystals. Microgravity created in space vehicles has provided a unique means by which the unwanted convective flows induced by gravity can be significantly suppressed, thereby offering an environment conductive to growing crystals with more uniform solute distribution and/or in a diffusion controlled regime. However, space experiments also reveal effects that are unknown or nonexistent on Earth. One of these effects is *g*-jitter or residual acceleration phenomena associated with space vehicles. Residual accelerations or *g*-jitter occurring during space processing of melts, such as the melts from which single crystals are grown, can cause appreciable convective flows, making it difficult to achieve diffusion controlled single crystal growth in space [1].

Gravity perturbation or *g*-jitter comes from crew motions, mechanical vibrations (pumps, motors, excitations of natural frequencies of spacecraft structures), spacecraft maneuvers and attitude, atmospheric drag and the Earth's gravity gradient [2]. Studies on *g*-jitter effects indicate that convection in microgravity is related

* Corresponding author. Tel.: +1-509-335-7386; fax: +1-509-335-4662.
E-mail address: li@mme.wsu.edu (B.Q. Li).

0017-9310/02/$ - see front matter
PII: S0017-9310(01)00137-5

Nomenclature

B_o, **b**	magnitude and direction (unit vector) of applied magnetic field
C	concentration
D	diffusivity
e	unit vector
f	frequency
g, g_o	gravity vector, gravity constant
Ha	Hartmann number
$\hat{i}, \hat{j}$	unit vector of ith, jth component
k	thermal conductivity
L	melt length
n	unit vector outnormal to the boundary
p, **P**	pressure, pressure at discretized nodal points
Pr	Prandtl number
Pe_g	Peclet number
q	flux
Ra	Rayleigh number
Sc	Schmidt number
t, **t**	time, unit vector tangential to the boundary
T^*, T	temperature, dimensionless temperature ($T = (T^* - T_m)/(T_h - T_m)$)
T_∞, T_r	temperature of surroundings, reference temperature
T_h, T_m	temperature of hot zone, melting temperature
T_{max}, T_{min}, **T**	maximum and minimum temperatures, temperature at discretized nodal points
ΔT	difference between T_{max} and T_{min}
u, **U**	velocity, velocity at discretized nodal points
V_g	growth velocity
$\hat{z}$	unit vector of z-direction
z	z coordinate

Greek symbols

β	thermal expansion coefficient
ε	penalty parameter
$\partial\Omega$	boundary of computational domain
∇	gradient operator
ϕ, ψ, θ	shape functions for velocity, pressure and scalars
κ	kinematic viscosity
λ	the solute segregation coefficient
μ	molecular viscosity
ρ	density
σ	electrical conductivity
Ω	computational domain

Subscripts

c	concentration
i, j	the ith, jth component
T	temperature

Superscripts

$*$	dimensional quantity
T	transpose

to the magnitude and frequency of g-jitter and to the alignment of the gravity field with respect to the growth direction or the direction of the temperature gradient [3–6]. A residual gravity of 10^{-5} g_o, where g_o is the Earth gravity constant, is sufficient to cause unacceptable fluid motion in the liquid. This g-jitter induced flow motion is intense enough to affect deleteriously the solute distribution in the melt and hence the quality of the crystals grown. The orientation of the gravity vector with respect to the temperature gradient also plays an important role in melt flows. The velocity attains a maximum when the gravity vector is perpendicular to the temperature gradient.

Numerous attempts have been made to estimate and calculate the adverse effects of time varying g-jitter [6–10]. These calculations are all based on numerical models. Both 2-D and 3-D numerical models have been developed for this purpose [4,12]. These models have been used to study the effects associated with both idealized single- and multiple-frequency g-jitter modulations and real g-jitter data collected by accelerometer during actual flight experiments. These studies showed that the frequency, amplitude and spatial orientation of the residual gravity vector all play an important role in determining the convective flow behavior of the system. When the residual accelerations oscillate about the positive and negative of an axis, the orientation of this direction relative to the density gradient determines whether a mean flow is generated in the system [11]. Sinusoidal accelerations induce an oscillating convective flow and composition oscillation in the liquid. The resulting velocity and composition fields oscillate with the same frequency as the affecting gravity field.

These studies have shed light on the basic nature of g-jitter effects and have provided a thrust to devise useful mechanisms to suppress g-jitter induced convective flows. One technique is to apply the principle of magnetic damping to achieve velocity reduction. Magnetic damping is less effective than reducing gravity for convection reduction. It originates from the interaction of the flow field of an electrically conducting fluid and an applied magnetic field. This interaction gives rise to an opposing Lorentz force that reduces or damps the flow velocities in the liquid. Application of a magnetic field has been found to be effective in controlling convection during crystal growth from melts under terrestrial con-

ditions and the technology is now widely practiced in the metals and semiconductor industries [13]. While there is a large amount of literature addressing both the basic characteristics of *g*-jitter induced flows and the application of magnetic damping to convection control in melt growth on Earth [13–15], little research work has been done on the assessment of the magnetic field effect on the convective flow associated with *g*-jitter in microgravity. Exceptions are the papers published by Ma and Walker [11] and Baumgartl and Muller [12,16], who have studied the magnetic damping effects on melt flow driven by *g*-jitter. The former presented a semi-analytical model for the magnetic field effects on *g*-jitter driven thermal convection, while the latter presented a 3-D model of melt flow driven by a single frequency *g*-jitter force parallel to the thermal gradient with either transverse or axial fields imposed. Their work showed that magnetic fields can be used to further reduce the melt induced by *g*-jitter and that higher magnetic fields and higher frequency produce smaller melt flow. While their work is of fundamental value in illustrating the magnetic field effects on *g*-jitter induced melt flows, critical issues remain essentially unresolved. Studies showed that unlike the case on Earth *g*-jitter can not be perfectly aligned with a thermal gradient. In fact, in a space environment, *g*-jitter changes in direction and the most deleterious flow effects result from the component perpendicular to the thermal gradient [4]. Also, melt flow in microgravity has little effect on thermal fields but has a very strong effect on the solutal transport. Moreover, *g*-jitter is random in nature and thus an accurate assessment of its effect in the presence of an external magnetic field should be made by taking into consideration its randomness in amplitude, direction and frequency.

In this paper, a numerical analysis is presented of magnetically-damped *g*-jitter driven flows and their effects on the solutal element distributions in a simplified 2-D Bridgman–Stockbarger crystal growth system. It should be noted that in actual crystal growth system in space, the flow structure is truly 3-D and 3-D models should be developed to fully appreciate the complex 3-D structure. Nonetheless, a 2-D analysis reveals some essential features of *g*-jitter induced flows and thus provides a basis upon which 3-D models can be developed. The 2-D analysis presented below is based on the solution of the Navier–Stokes equations for fluid flow, the energy balance equation for the temperature distribution and the mass balance equation for species transport in a Ga-doped germanium melt. Numerical simulations are conducted of the transient convective flows and solutal redistribution in the melts under the combined action of *g*-jitter and external magnetic fields. In what follows, the numerical model development is described. The model is checked against available analytical solutions for simplified conditions. Analysis is made of the magnetic damping effects on the flow and mass transfer induced by both idealized single frequency *g*-jitter and also the real *g*-jitter measurements taken during a space flight. As is shown below, the *g*-jitter induced flows have more pronounced effects on mass transport and hence the magnetic field can be very effective in smoothing out concentration variation in the liquid.

2. Problem statement

Fig. 1 shows a simplified 2-D version of the Bridgman–Stockbarger single crystal growth process under microgravity conditions, along with the coordinate system for analyses. This configuration is chosen because it has been considered for space applications and numerical simulations using this configuration have been conducted by Alexander et al. [4] for melt flows and solute transport in a *g*-jitter environment without an applied magnetic field. The crystal–melt interface is located at $y = 0$ and the melt is fed into the melt pool of height L from above. The width of the cavity is W, which is set equal to the height. The temperature at the crystal–melt interface is kept at T_m, and that at the inlet and the upper side walls is held at a higher temperature T_h. The lower side walls are adiabatic zones. The origin of the coordinate system is at the lower left corner of the cavity. In practice the solidification of a dilute two-component melt takes place as the ampoule is translated through fixed hot and cold zones. The translation of the ampoule is simulated by supplying a doped melt of bulk composition c and density ρ at a constant velocity V_g at the top of the computational space (inlet). The ampoule is fed into the melt zone and the solidified alloy of composition c_s is withdrawn from below [4].

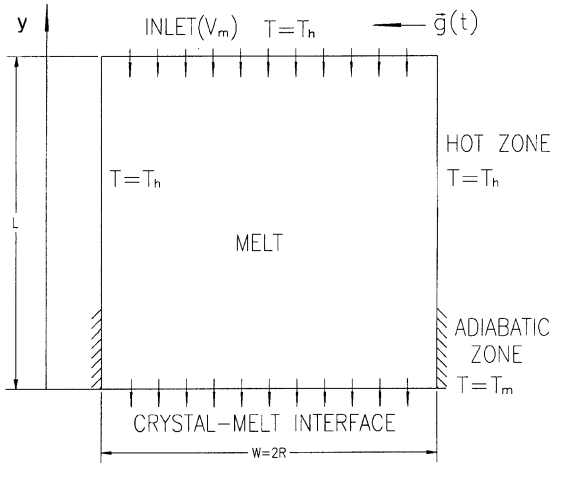

Fig. 1. Schematic representation of the natural convection problems in a 2-D cavity in a microgravity environment.

In a typical microgravity environment, the residual acceleration experienced by the spacecraft is composed of a steady component and a time-dependent component. The magnitude of the time-dependent component is much greater than that of the steady component. In this paper we consider the time dependent acceleration (g-jitter) represented by the following expression,

$$\mathbf{g}^*(t^*) = \sum_{n=1}^{N} \mathbf{g}_n^* \sin(2\pi f_n^* t^*)\mathbf{e}. \tag{1}$$

Here the asterisks designate the dimensional quantities. The direction of the residual gravity is set to be parallel to the crystal–melt interface in the present work, which has the most detrimental effects in terms of convective flows [4]. We also consider the real g-jitter data taken during a space flight. The above crystal growth system is immersed in a DC magnetic field in the y-direction, which is intended to damp the g-jitter induced convection.

Our primary objective is to study the g-jitter-driven melt flow and the effect of the magnetic field on the flow in the system as described above. As a first approximation, the solidification phenomena are not considered in the present study and thus the melt–crystal interface is held flat. The melt flow, heat and mass transport in the 2-D cavity as illustrated in Fig. 1 are governed by the continuity equation, the Navier–Stokes equations, the energy balance equation and the species conservation equation in the presence of an external magnetic field. These equations may be written in a nondimensionalized form as follows [17,18]:

$$\nabla \cdot \mathbf{u} = 0 \tag{2}$$

$$\frac{\partial \mathbf{u}}{\partial t} + \mathbf{u}\cdot\nabla\mathbf{u} = -\nabla p + Pr\nabla^2\mathbf{u} - RaPr\mathbf{g}(t)\theta + Ha^2 Pr(\mathbf{u}\times\mathbf{b}\times\mathbf{b}), \tag{3}$$

$$\frac{\partial T}{\partial t} + \mathbf{u}\cdot\nabla T = \nabla^2 T, \tag{4}$$

$$\frac{Sc}{Pr}\left(\frac{\partial C}{\partial t} + \mathbf{u}\cdot\nabla C\right) = \nabla^2 C. \tag{5}$$

The last term in Eq. (3) represents the effect of the Lorentz force that arises from the application of an external magnetic field. In deriving the above equations, the following scales are used: κ/L for velocity, L for length, L^2/κ for time, $\rho\kappa^2/L^2$ for pressure and g_0 for gravity. Furthermore, $\mathbf{g}(t)$ can be expressed as

$$\mathbf{g}(t) = \sum_{n=1}^{N} g_n \sin(2\pi f_n t)\mathbf{e}, \tag{6}$$

where f_n is scaled by κ/L^2. The dimensionless parameters are defined as

$$Ra = \frac{\beta g_0 (T_h - T_m)L^3}{\nu\kappa}, \quad Ha = B_0 L\sqrt{\frac{\sigma}{\mu}}, \quad Pr = \frac{\nu}{\kappa}, \quad Pe_g = \frac{V_g L}{D}, \quad Sc = \frac{\nu}{D}. \tag{7}$$

The boundary conditions for the system under consideration are given by

$$\theta = 0, \quad \mathbf{u}\cdot\mathbf{n} = \frac{Pe_g Pr}{Sc}, \quad \mathbf{u}\times\mathbf{n} = 0, \quad \mathbf{n}\cdot\nabla C = Pe_g(1-\lambda)C \quad \text{at } Y = 0, \tag{8}$$

$$\theta = 1, \quad \mathbf{u}\cdot\mathbf{n} = -\frac{Pe_g Pr}{Sc}, \quad \mathbf{u}\times\mathbf{n} = 0, \quad \mathbf{n}\cdot\nabla C = -Pe_g(C-1) \quad \text{at } Y = 1, \tag{9}$$

$$\mathbf{u}\cdot\mathbf{t} = -\frac{Pe_g Pr}{Sc}, \quad \mathbf{u}\cdot\mathbf{n} = 0, \quad \mathbf{n}\cdot\nabla C = 0;$$

along the two sides $\theta = 1$ along the hot zone side; and $\mathbf{n}\cdot\nabla T = 0$ along the adiabatic zone.

3. The finite element solution

The above governing equations along with the boundary conditions are solved using the Galerkin finite element method. The stiffness matrix is obtained by using Galerkin's method of Weighted Residuals. Following the procedures given in [17,19], the governing equations are recast in integral forms

$$\left(\int_\Omega \psi \hat{i}\cdot\nabla\phi^{\mathrm{T}}\,\mathrm{d}V\right)\mathbf{U}_i = -\varepsilon\left(\int_\Omega \psi\psi^{\mathrm{T}}\,\mathrm{d}V\right)\mathbf{P}, \tag{10}$$

$$\left(\int_\Omega \phi\phi^{\mathrm{T}}\,\mathrm{d}V\right)\frac{\mathrm{d}\mathbf{U}_i}{\mathrm{d}t} + \left(\int_\Omega \phi\mathbf{u}\cdot\nabla\phi^{\mathrm{T}}\,\mathrm{d}V\right)\mathbf{U}_i - \left(\int_\Omega \hat{i}\cdot\nabla\phi\psi^{\mathrm{T}}\,\mathrm{d}V\right)\mathbf{P} + \left(\int_\Omega Pr\nabla\phi\cdot\nabla\phi^{\mathrm{T}}\,\mathrm{d}V\right)\mathbf{U}_i + \left(\int_\Omega Pr(\hat{i}\cdot\nabla\phi)(\hat{j}\cdot\nabla\phi^{\mathrm{T}})\,\mathrm{d}V\right)\mathbf{U}_j + \left(\int_\Omega RaPr\phi\theta^{\mathrm{T}}\mathbf{g}\,\mathrm{d}V\right)\mathbf{T} = \int_{\partial\Omega}\mathbf{n}\cdot\tau\cdot\hat{i}\phi\,\mathrm{d}S + \int_\Omega \phi Ha^2 Pr(\mathbf{u}\times\mathbf{b}\times\mathbf{b})\,\mathrm{d}V, \tag{11}$$

$$\left(\int_\Omega \theta\theta^{\mathrm{T}}\,\mathrm{d}V\right)\frac{\mathrm{d}\mathbf{T}}{\mathrm{d}t} + \left(\int_\Omega \theta\mathbf{u}\cdot\nabla\theta^{\mathrm{T}}\,\mathrm{d}V\right)\mathbf{T} + \left(\int_\Omega \nabla\theta\cdot\nabla\theta^{\mathrm{T}}\,\mathrm{d}V\right)\mathbf{T} = -\int_{\partial\Omega} q_{\mathrm{T}}\theta\,\mathrm{d}S, \tag{12}$$

$$\left(\int_\Omega \frac{Sc}{Pr}\theta\theta^{\mathrm{T}}\,\mathrm{d}V\right)\frac{\mathrm{d}\mathbf{C}}{\mathrm{d}t} + \left(\int_\Omega \frac{Sc}{Pr}\theta\mathbf{u}\cdot\nabla\theta^{\mathrm{T}}\,\mathrm{d}V\right)\mathbf{C} + \left(\int_\Omega \nabla\theta\cdot\nabla\theta^{\mathrm{T}}\,\mathrm{d}V\right)\mathbf{C} = -\int_{\partial\Omega} q_c\theta\,\mathrm{d}s. \tag{13}$$

Once the form of shape functions ϕ, θ, and ψ are specified, the integrals defined in the above equations can be expressed in matrix form. Combining the mo-

mentum and energy equations into a single matrix equation gives rise to the following element stiffness matrix equation:

$$\begin{bmatrix} \mathbf{M} & 0 & 0 \\ 0 & \mathbf{N}_T & 0 \\ 0 & 0 & \mathbf{N}_C \end{bmatrix} \begin{bmatrix} \dot{\mathbf{U}} \\ \dot{\mathbf{T}} \\ \dot{\mathbf{C}} \end{bmatrix} + \begin{bmatrix} \mathbf{A}(\mathbf{U}) + \mathbf{K} + \frac{1}{\varepsilon}\mathbf{E}\mathbf{M}_p^{-1}\mathbf{E}^{\mathrm{T}} & \mathbf{B} & 0 \\ 0 & \mathbf{D}_T(\mathbf{U}) + \mathbf{L}_T & 0 \\ 0 & 0 & \mathbf{D}_C(\mathbf{U}) + \mathbf{L}_C \end{bmatrix} \times \begin{bmatrix} \mathbf{U} \\ \mathbf{T} \\ \mathbf{C} \end{bmatrix} = \begin{bmatrix} \mathbf{F} \\ \mathbf{G}_T \\ \mathbf{G}_C \end{bmatrix}. \tag{14}$$

Note that in constructing the above element matrix equation, the penalty formulation has been applied, and $\mathbf{P}$ in the momentum equation is substituted by $\frac{1}{\varepsilon}\mathbf{M}_p^{-1}\mathbf{E}^{\mathrm{T}}\mathbf{U}$. The assembled global matrix equations are stored in the skyline form and solved using the Gaussian elimination method. The coefficient matrices of Eq. (14) above are calculated by

$$\mathbf{M}_p = \int_\Omega \psi\psi^{\mathrm{T}}\,\mathrm{d}V,$$

$$\mathbf{N}_T = \int_\Omega \theta\theta^{\mathrm{T}}\,\mathrm{d}V,$$

$$\mathbf{M} = \int_\Omega \theta\theta^{\mathrm{T}}\,\mathrm{d}V,$$

$$\mathbf{N}_C = \int_\Omega \frac{Sc}{Pr}\theta\theta^{\mathrm{T}}\,\mathrm{d}V,$$

$$\mathbf{E}_i = \int_\Omega \widehat{i}\cdot\nabla\phi\psi^{\mathrm{T}}\,\mathrm{d}V,$$

$$\mathbf{L}_C = \int_\Omega \nabla\theta\cdot\nabla\theta^{\mathrm{T}}\,\mathrm{d}V,$$

$$\mathbf{L}_T = \int_\Omega \nabla\theta\cdot\nabla\theta^{\mathrm{T}}\,\mathrm{d}V,$$

$$\mathbf{A}(\mathbf{U}) = \int_\Omega \phi u\cdot\nabla\theta^{\mathrm{T}}\,\mathrm{d}V,$$

$$\mathbf{D}_C(\mathbf{U}) = \int_\Omega \frac{Sc}{Pr}\theta\mathbf{u}\cdot\nabla\theta^{\mathrm{T}}\,\mathrm{d}V,$$

$$\mathbf{D}_T(\mathbf{U}) = \int_\Omega \theta\mathbf{u}\cdot\nabla\theta^{\mathrm{T}}\,\mathrm{d}V,$$

$$\mathbf{B} = \int_\Omega (RaPr\mathbf{g}\phi\theta^{\mathrm{T}})\,\mathrm{d}V,$$

Table 1
Parameters used in calculations

Property	Value
Thermal conductivity of the melt (k)	17 W K^{-1} m^{-1}
Heat capacity of the melt (C_p)	0.39 J g^{-1} K^{-1}
Density of the melt (ρ)	5.6×10^3 kg m^{-3}
Kinematic viscosity of the melt (v)	1.3×10^{-7} m^2 s^{-1}
Solute diffusivity (D)	1.3×10^{-8} m^2 s^{-1}
Thermal diffusivity of the melt (κ)	1.3×10^{-5} m^2 s^{-1}
Thermal expansion coefficient (β)	2.5×10^{-4} K^{-1}
Dimensionless parameters	*Value*
Prandtl number (Pr)	0.01
Peclet number (Pe)	5.0
Rayleigh number (Ra)	1.45×10^5 (on the Earth value)
Hartmann number (Ha)	10–100
Schmidt number (Sc)	10
Scale parameters	*Value*
Velocity scale ($U_o=\kappa/L$)	1.3×10^{-3}
Time scale ($t_o=L^2/\kappa$)	100/13
Frequency scale ($f_o=\kappa/L^2$)	0.13
Operating conditions	*Value*
Hot zone temperature (T_h)	1331 K
Distance between inlet and interface (L)	0.01 m
Interface temperature (T_m)	1231 K
Translation rate (V_m)	6.5×10^{-6} m s^{-1}
Gravity (g)/frequency (Hz)	$10^{-3}g_0/0.1$
Magnetic field B_0	0.022–0.22 T

$* \ 1g_0 = 9.8$ m s^{-2}.

$$\mathbf{G}_C = -\int_{\partial\Omega} q_C \theta \, \mathrm{d}S,$$

$$\mathbf{G}_T = -\int_{\partial\Omega} q_T \theta \, \mathrm{d}S,$$

$$\mathbf{F} = \int_{\partial\Omega} \mathbf{n} \cdot \tau\phi \, \mathrm{d}S + \int_{\Omega} \phi Ha^2 Pr(\mathbf{u} \times \mathbf{b} \times \mathbf{b}) \, \mathrm{d}V,$$

$$\mathbf{K}_{ij} = \left(\int_{\Omega} Pr \nabla\phi \cdot \nabla\phi^{\mathrm{T}} \, \mathrm{d}V \right) \delta_{ii} + \int_{\Omega} Pr(\hat{i} \cdot \nabla\phi)(\hat{j} \cdot \nabla\phi^{\mathrm{T}}) \, \mathrm{d}V.$$

4. Results and discussion

The transient finite element model described above enables the prediction of the transient convective flows

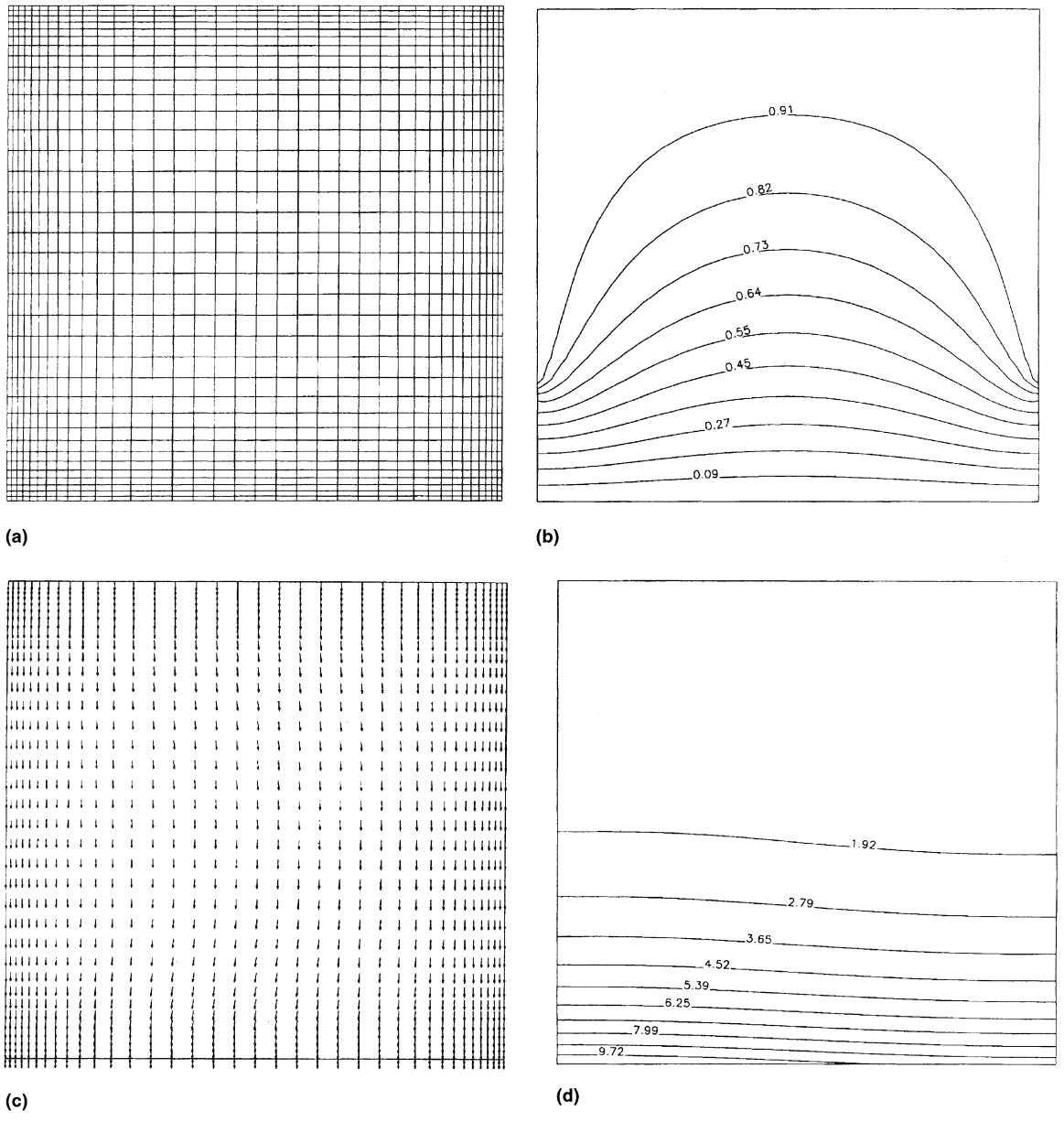

Fig. 2. Meshes and initial conditions for transient simulations: (a) finite element mesh used for computation, (b) thermal profile, (c) initial velocity profile ($U_{\max} = 0.005536$), and (d) initial isoconcentration profile. The initial profiles are the steady state fluid flow, thermal and solute distributions caused by $g = 1 \times 10^6 g_0$ acting in the x-direction.

driven by *g*-jitter, the temperature distribution and the solutal redistribution in the melt with and/or without an applied magnetic field. The calculations were performed using a finite element code that was developed by our research group. The code employs the backward Euler (or implicit) time difference scheme, with automatic time step control, and the penalty method for pressure approximation. The computer code was checked against other available commercial codes for fluid flow and thermal calculations, including FIDAP and FLUENT, and analytical solutions for a wide variety of flows and thermal problems. A selection of computed results is presented below and the parameters used for calculations are given in Table 1 [4]. Unless otherwise indicated, the transient calculations begin with an initial thermal and fluid flow field obtained with a constant gravity field of $g = 1 \times 10^{-6} g_0$ acting in the direction perpendicular to the growth direction. The external magnetic fields for all the calculations are oriented parallel to the *y*-direction.

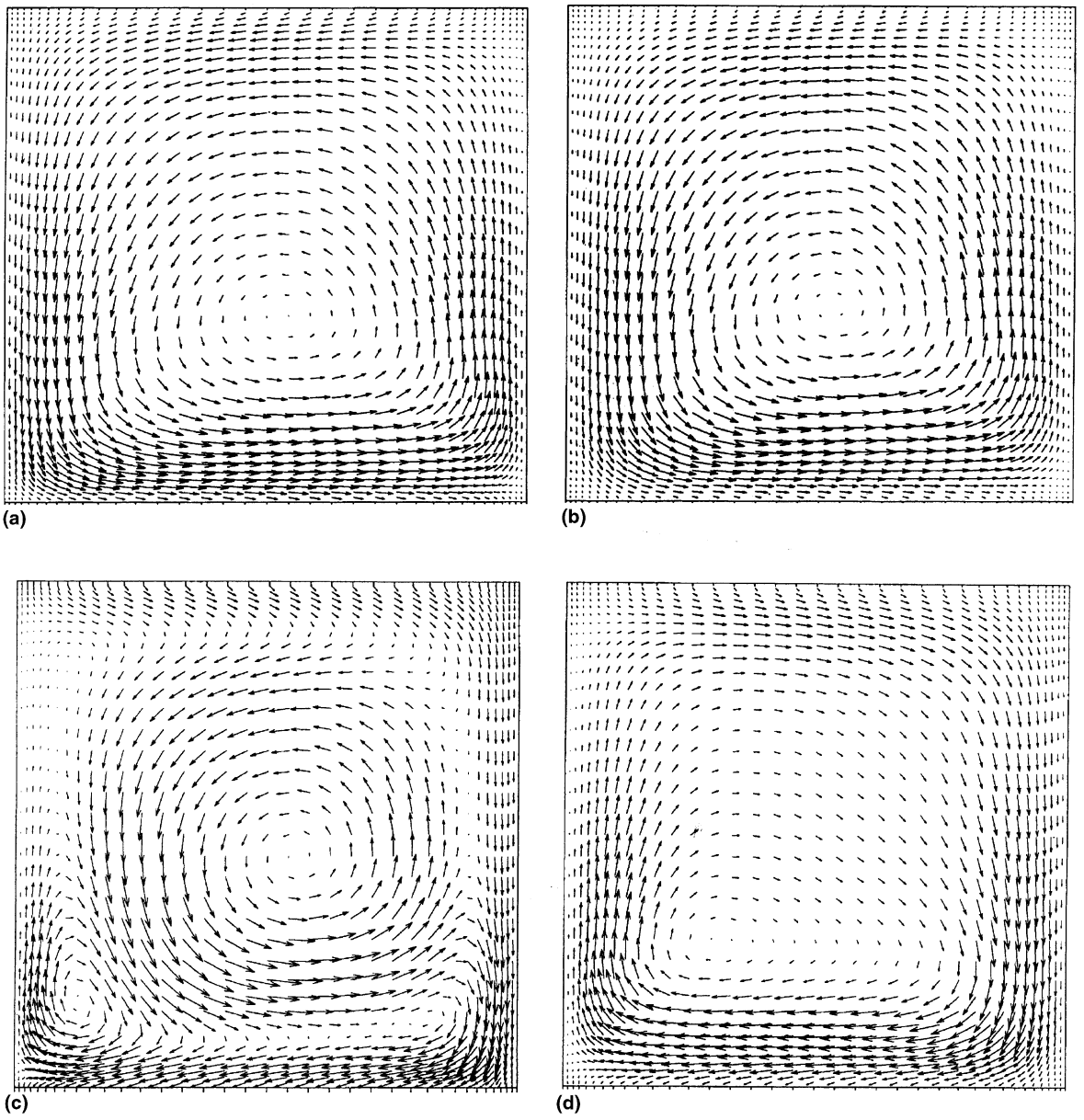

Fig. 3. The dynamic development of the velocity field caused by a time varying *g*-jitter driving force in the absence of a magnetic field: (a) $t = 0.325$, $U_{max} = 0.09797$; (b) $t = 0.65$, $U_{max} = 0.1425$; (c) $t = 0.975$, $U_{max} = 0.04124$; and (d) $t = 1.3$, $U_{max} = 0.06911$.

To further assess the code predictability for the magnetic damping effects on g-jitter driven flows, the finite element results were compared with the analytical solutions obtained for convective flows in a simple parallel plate geometry subject to a transverse magnetic field [20]. The analytical solution is obtained by assuming that the fluid is pumped through a long channel by an oscillating buoyancy force in the presence of a transverse magnetic field and that the channel is long enough to ensure a 1-D flow with end effects neglected. To ensure the comparison between the numerical and analytical solutions, the height-to-width aspect ratio was set at 5, which was found to be sufficient to simulate the infinitely long parallel plate geometry. It was found that the numerical results are in excellent agreement with the analytical solutions for this idealized system. The details of the comparison are documented in a recent thesis [17].

Studies based on analytical solutions [20] further suggest that in the presence of a magnetic field, the Hartmann layer develops near the solid boundary. For a flow driven by oscillating forces, the Hartmann layer is

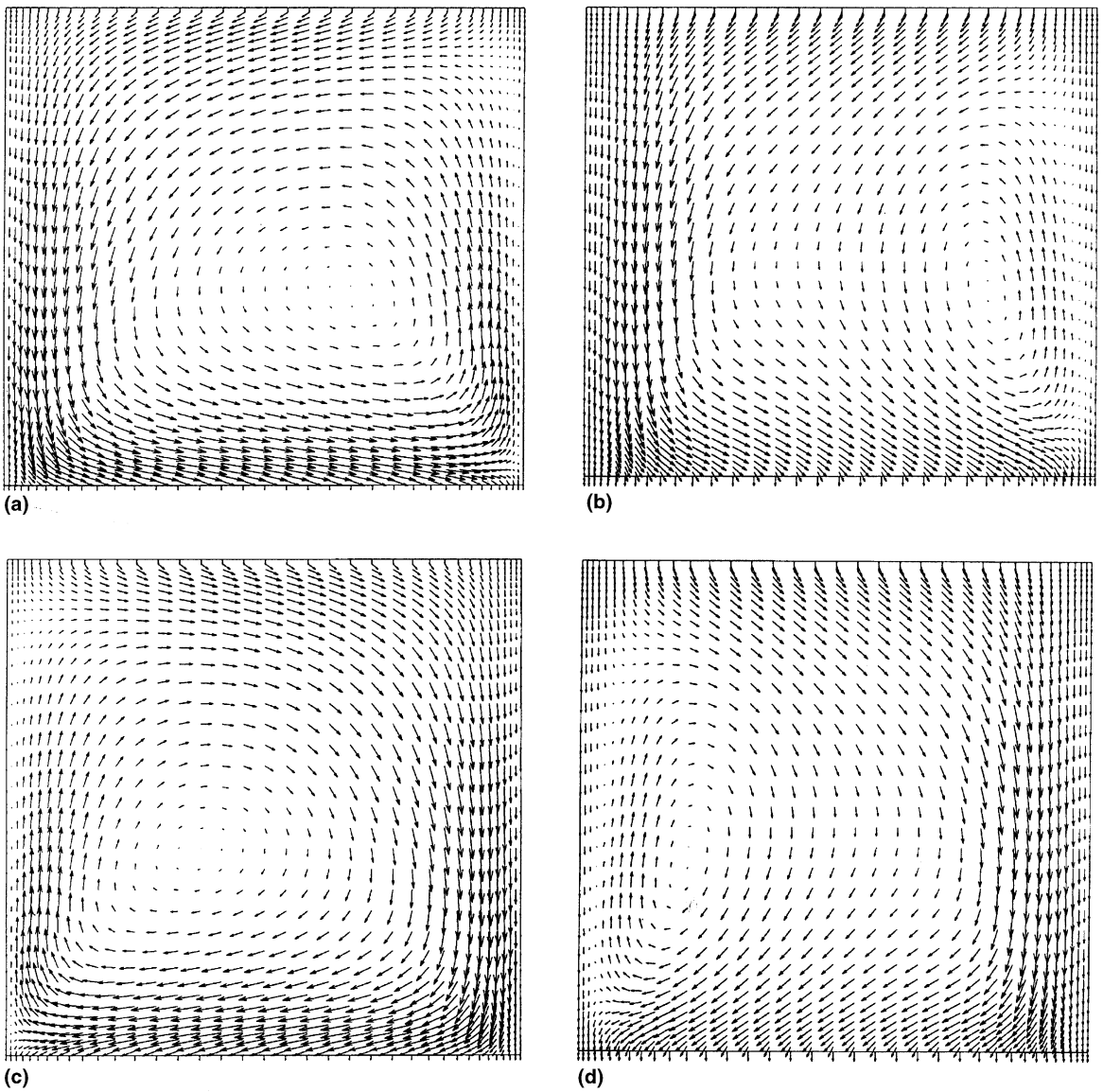

Fig. 4. The evolution of a magnetically damped flow field driven by a time varying g-jitter component with an applied magnetic field $Ha = 50$ and other conditions the same as in Fig. 6: (a) $t = 0.325$, $U_{max} = 0.03633$; (b) $t = 0.65$, $U_{max} = 0.01803$; (c) $t = 0.975$, $U_{max} = 0.03576$; and (d) $t = 1.3$, $U_{max} = 0.01778$.

dependent upon both the frequency of the oscillating forces and the applied magnetic field strength [20]. In general, the Hartmann layer is thinner for an oscillating force than for a constant force. These analytical solutions serve as a good guideline for developing finite element meshes for numerical simulations. Mesh dependence is tested for a flow with a Hartmann number of 100, which represents the worst scenario to be studied in this paper. Various mesh distributions were used. It was found that the flow field is modeled well with four 4-node finite elements in the Hartmann boundary layer. The results remain basically the same with a further increase in number of elements in the Hartmann layer. Based on this testing, a mesh of 1296 4-node finite elements was used, as shown in Fig. 2(a), for the computed results presented below.

With the finite element model described above, the *g*-jitter driven flows, thermal field and solutal

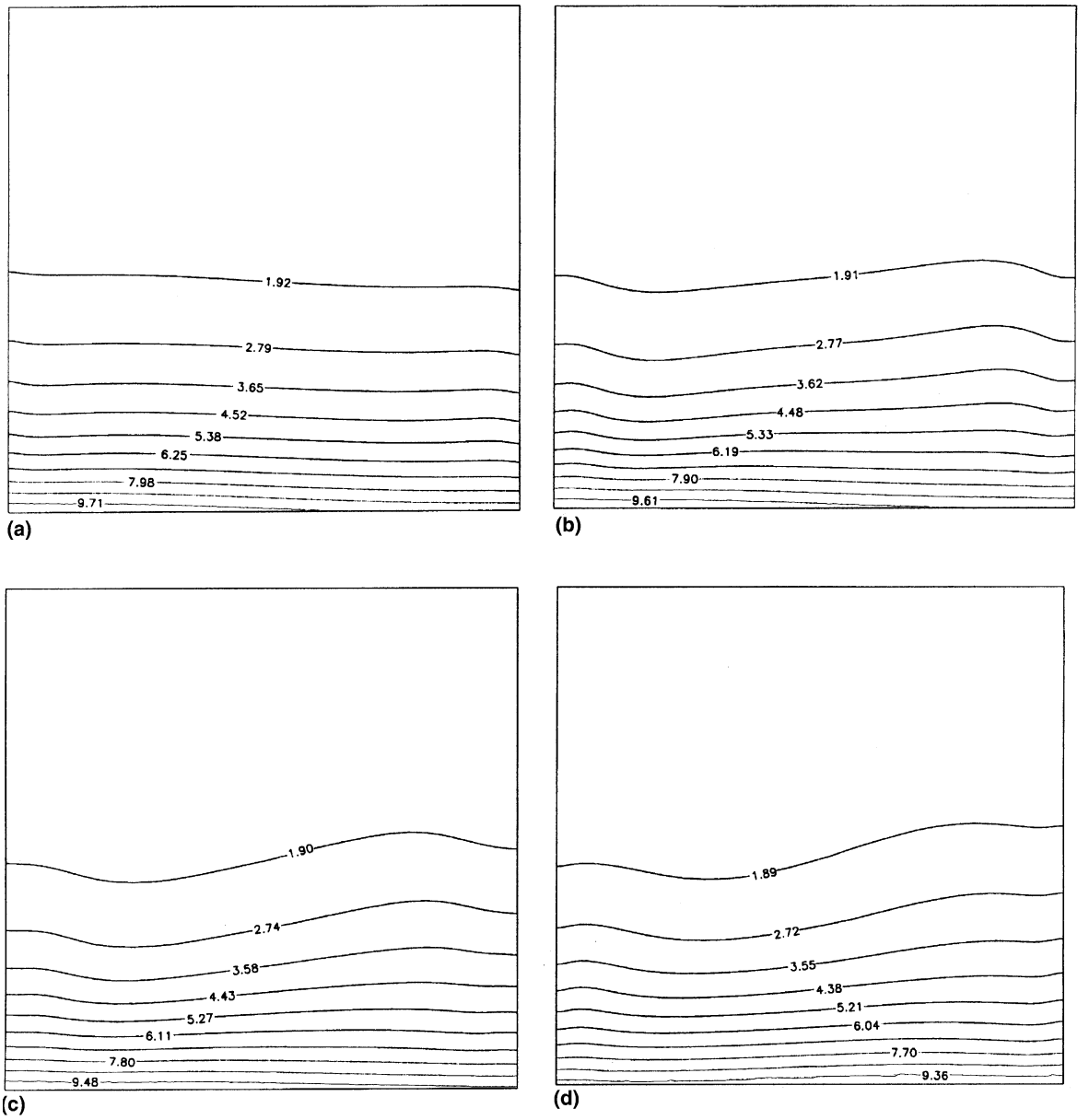

Fig. 5. Time variation of concentration distribution in the melt in the absence of an applied magnetic field: (a) $t = 0.325$, (b) $t = 1.3$, (c) $t = 2.925$, and (d) $t = 11.7$.

redistribution in the system can be analyzed. Fig. 2(b) depicts the computed temperature distribution in the system. For all the cases studied, the temperature profile remains basically the same and is practically unaffected by natural convection in the pool. This is as expected because the Prandtl number is small for the melt being studied ($Pr = \nu/\kappa = 0.01$); thus thermal transport is dominated by conduction. The fluid flow and solute transport, however, are strongly dependent upon the g-jitter characteristics and the applied magnetic field.

To model the effect of g-jitter perturbation on the fluid flow, the space flight is first envisioned to be in an undisturbed condition that permits steady state natural convection and then g-jitter sets in to perturb the existing fluid flow field. The steady state fluid flow field and temperature and solute distributions, which are used as initial conditions for transient calculations presented below, are

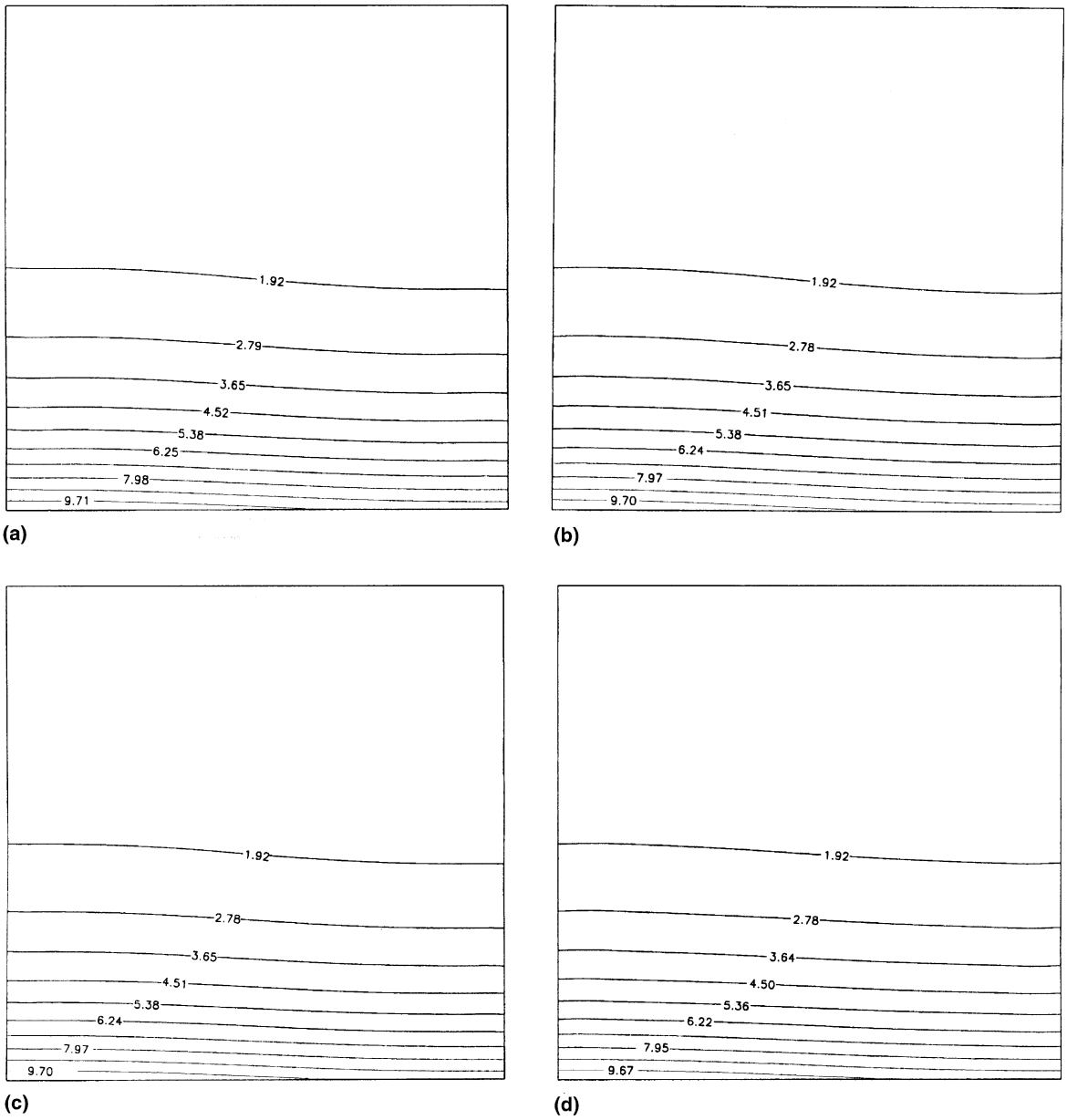

Fig. 6. Time variation of concentration distribution in the melt with an applied magnetic field $Ha = 100$: (a) $t = 0.325$, (b) $t = 1.3$, (c) $t = 2.925$, and (d) $t = 11.7$.

calculated using a constant microgravity force acting perpendicular to the y-direction, as stated earlier. This orientation was chosen because it produces the most severe effects on the fluid flow fields [4–6]. The calculated results are shown in Fig. 2(c) and (d). Note that Alexander et al. [4] also did the same calculations using the spectral method and our results are the same as theirs; thereby providing a further verification on our calculations.

Fig. 3 illustrates a set of dynamically developing melt flow recirculation patterns that evolved from those depicted in Fig. 2(c) and (d) when a single frequency g-jitter perturbation sets in. The perturbation is assumed to oscillate in time harmonically and follows a sine function, $g^*(t^*) = 10^{-3} g_0 \sin(0.2\pi t^*)$. Clearly, the fluid flow field is dominated by a single recirculating loop over the entire cavity and the flow loop oscillates in

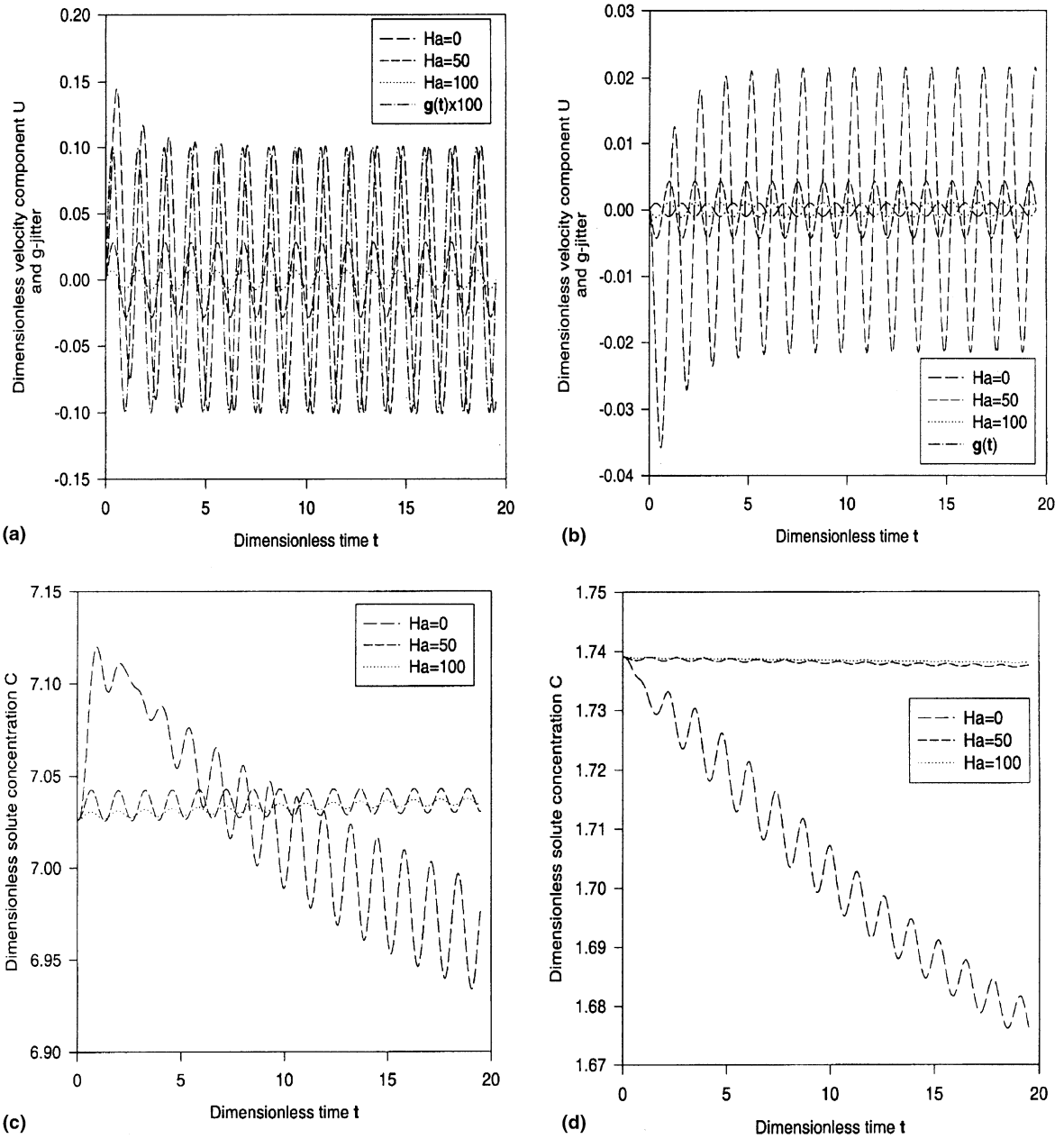

Fig. 7. The effects of a magnetic field on the oscillation of velocities and concentration at some points in the liquid pool with single frequency g-jitter: (a and c) at point ($x = 0.5,\ y = 0.08$); (b and d) at point ($x = 0.5,\ y = 0.5$).

direction in response to the *g*-jitter driving force. Fig. 3(c) captures the moment at which the reversal of the gravity force causes the anti-clockwise rotation to be replaced by the emerging, clockwise rotating flow cell. Comparison of Fig. 3(a) and (d) shows that the rotation is completely reversed over the first oscillation period. Further analysis indicates that for this case the flow field evolves to a quasi-steady state with a defined frequency approximately five irregular periods after *g*-jitter sets in.

A set of evolving fluid flow cells is calculated using the same conditions as those in Fig. 3 but with an applied magnetic field. The results are plotted in Fig. 4 for one oscillation period corresponding to that in

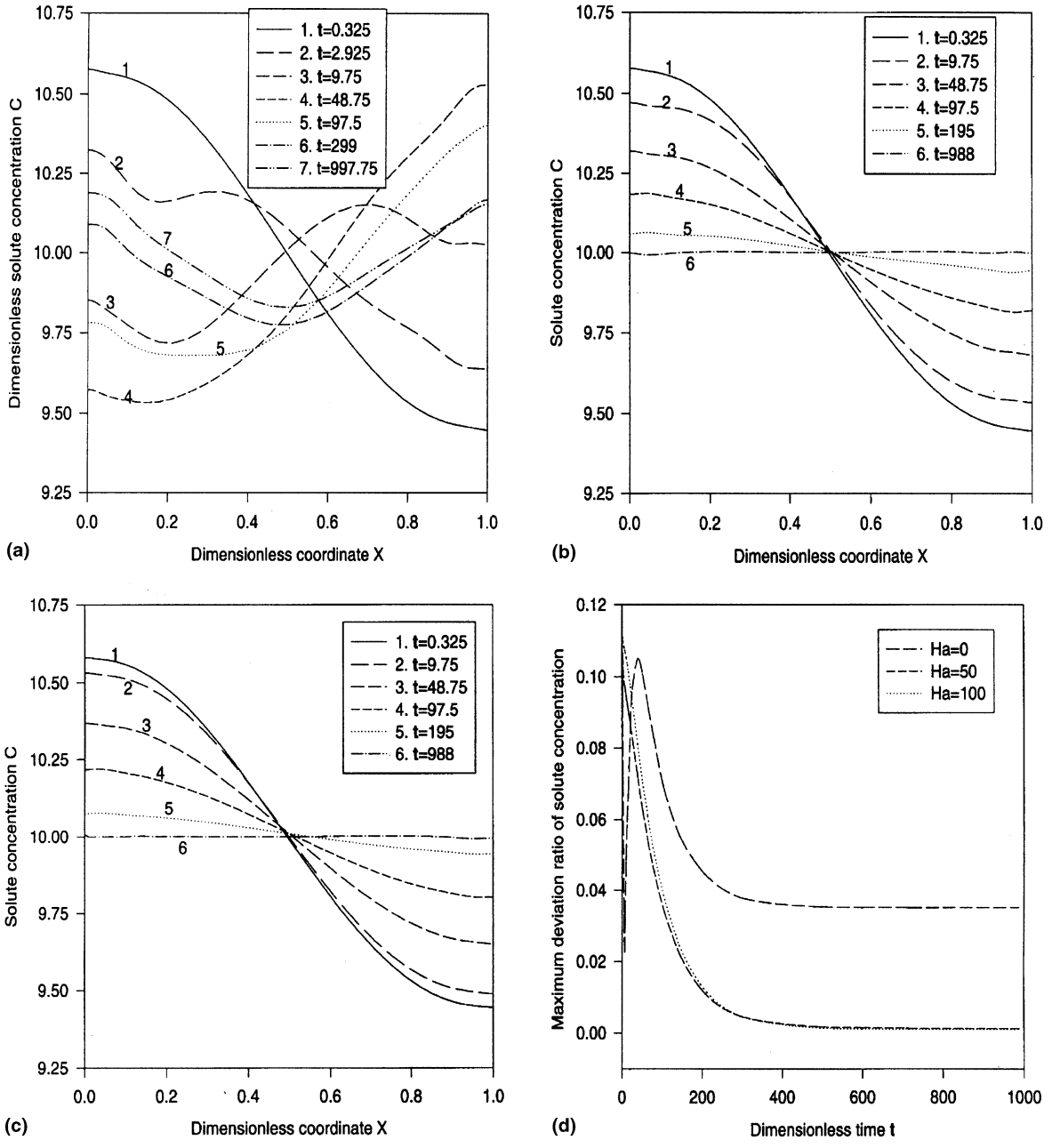

Fig. 8. Time variation of solutal distribution along the solid–liquid interface ($y = 0$) in the presence of magnetic fields: (a) $Ha = 0$, (b) $Ha = 50$, (c) $Ha = 100$, and (d) maximum deviation ratio of solute concentration.

Fig. 3. In this case, the magnetic field is applied in the y-direction when g-jitter becomes active. Unless otherwise indicated, the same is also assumed for other cases discussed below. In comparison with Fig. 3, it is clear that with an applied magnetic field, the flow intensity is reduced and the maximum velocity becomes smaller. The flow evolution pattern is also different. Over the first period when g-jitter is on, the flow exhibits a regular repetition in rotation directions and flow cell structure, as indicated by Fig. 4(a) and (c). Results of velocities obtained for other ensuing time periods show basically the same transient behavior. Additional simulations indicate that an increase in magnetic field strength further reduces the magnitude of the velocity and shifts the phase angle, but it does not change the basic pattern of the oscillating fluid flow field.

The convection in the liquid pool can have a significant effect on the solutal distribution during crystal growth. To investigate this effect in an oscillating flow field, the time dependent concentration profiles in the melt are plotted in Figs. 5 and 6 with and without a magnetic field applied, respectively. From Fig. 5, it is apparent that in the absence of an applied field, the concentration profile evolves as velocity changes and the g-jitter induced flow strongly affects the solutal transport in the melt. This is in contrast with Fig. 6, where the transient development of concentration profiles is shown in the presence of an external magnetic field. Obviously, the solute striation is much reduced, which is a direct consequence of the reduction of convection by the applied magnetic field.

To further investigate the effect of the magnetic field on the single frequency g-jitter induced flows, the velocity and solute oscillations are plotted in Fig. 7 as a function of time at some specific locations in the melt pool. As a comparison, the driving g-jitter force $(g(t))$ is also plotted. Important features of flow behavior may be summarized as follows. First, the flows oscillate with the same frequency as the driving force. This holds true whether or not an external magnetic field is present. The flow intensity is suppressed by an external magnetic field. A higher magnetic field produces a more pronounced damping effect. Second, the g-jitter induced flows lag behind the driving force and the phase angle varies with geometric locations. The application of a magnetic field changes the phase angles but not the frequency. A higher magnetic field causes the melt to oscillate more closely in phase (see Fig. 7(a)) with the frequency of the driving g-jitter. Finally, with applied magnetic fields, the time over which flow develops into a quasi-steady state is shortened. For the results shown, the flow reaches a quasi-steady state after only one period of oscillation with applied magnetic fields, whereas it takes approximately five oscillation periods when a magnetic field is absent.

Examination of the results in Fig. 7 also shows that shortly after the g-jitter perturbation sets in the concentration field is severely disturbed by the flow field. Afterwards, the concentration oscillates at the same frequency as the flow and gradually approaches to a steady state mean value. With an applied magnetic field, the concentration field quickly reaches a quasi-steady state and oscillates around a stable mean value. The

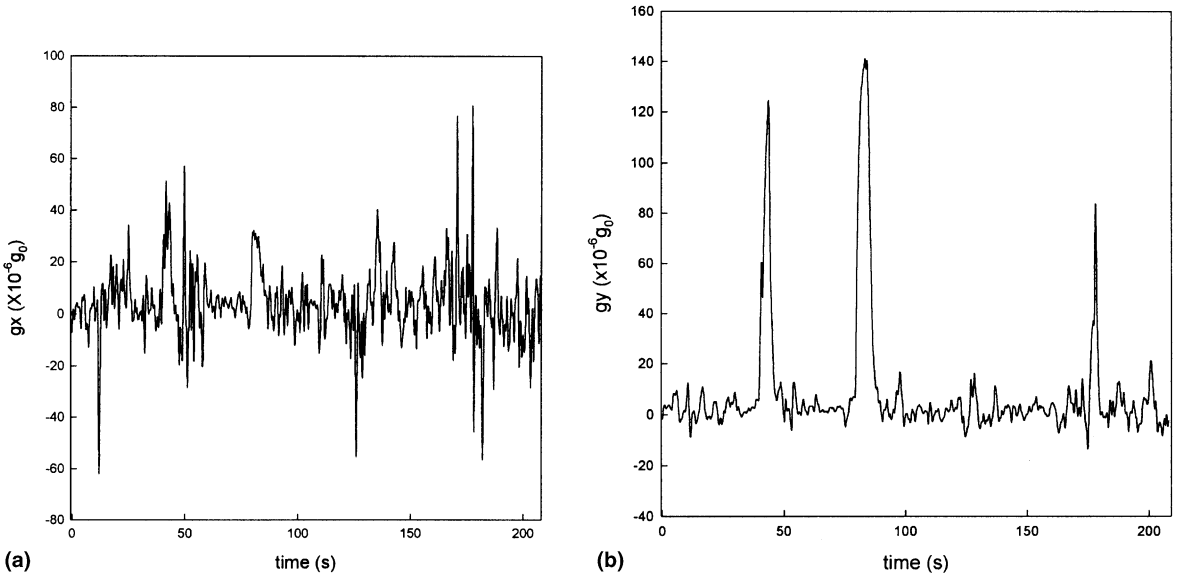

Fig. 9. Signature of g-jitter data in the x and y directions as a function of time registered by an accelerometer aboard the Space Shuttle, where time is measured in seconds.

amplitude of the oscillation is also reduced significantly with an applied magnetic field, suggesting that the local variation of the concentration becomes smaller because of reduced flow intensity. Also, a stronger magnetic field is more effective in reducing the concentration variation.

The effect of an applied magnetic field on the concentration field is further illustrated in Fig. 8, where the solutal distribution along the solid–liquid interface ($y = 0$) is plotted as a function of time. In the absence of an external field, a strong striation of the concentration across the interface exists and evolves with time. The oscillating convective flows force the concentration to change above and below the mean value of 10 (dimensionless), as seen in Fig. 8(a). There is a drastic variation across the interface

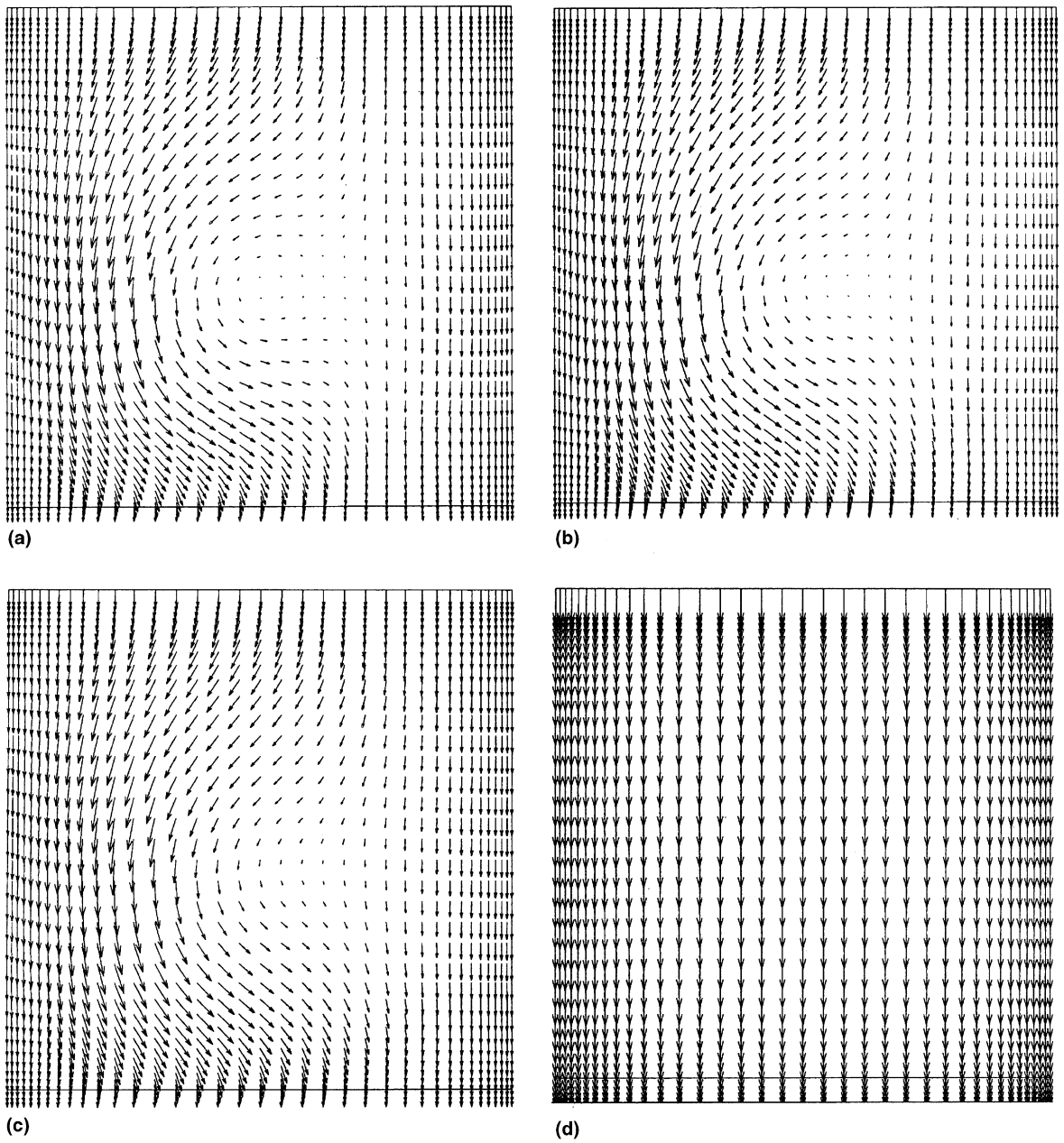

Fig. 10. Time development of a real g-jitter induced velocity field in the presence of an applied magnetic field: (a) $t = 12.22$, $Ha = 0$; (b) $t = 12.48, Ha = 0$; (c) $t = 12.74, Ha = 0$; and (d) $t = 12.22$–$12.48, Ha = 50$.

during the first 154 cycles of oscillation (dimensionless time $t = 0$–200). The striation decreases and finally settles at 0.04 after t = 455 (or 350 cycles of oscillation), as shown in Fig. 8(d). With applied magnetic fields, the solutal striation across the solid–liquid interface is greatly reduced. Furthermore, the solutal striation decreases with an increase in the applied field strength (see Fig. 8(b) and (c)). There exists also a period over which concentration changes drastically across the interface. However, the deviation (|maximum-minimum|/mean) reduces to about 0.04 within $t = 100$ and finally settles at a value of 0.002, in the presence of magnetic fields.

Inspection of the velocity results shown above and those obtained by additional simulations suggests that the velocity field in general may be approximately represented by $\mathbf{U}(x, y; t) = \mathbf{U}_{\mathrm{am}}(x, y)\sin(\omega t + \phi)$ where $\mathbf{U}_{\mathrm{am}}(x, y)$ is the amplitude and ϕ is the phase angle, which is a function of location and velocity components. This is also consistent with the conclusions obtained based on the analytical solutions [20]. As a result, $\mathbf{U}_{\mathrm{am}}$ may be used as an indicator of the velocity intensity. Simulations show that the flow amplitude, $\mathbf{U}_{\mathrm{am}}$, is approximately proportional to the amplitude of the g-jitter perturbation and it decreases with an increase in the applied magnetic field. With the same magnetic field strength, the damping effects are pronounced on the velocity field with higher amplitudes.

Numerical simulations have also been carried out for a range of frequencies and amplitudes. For the

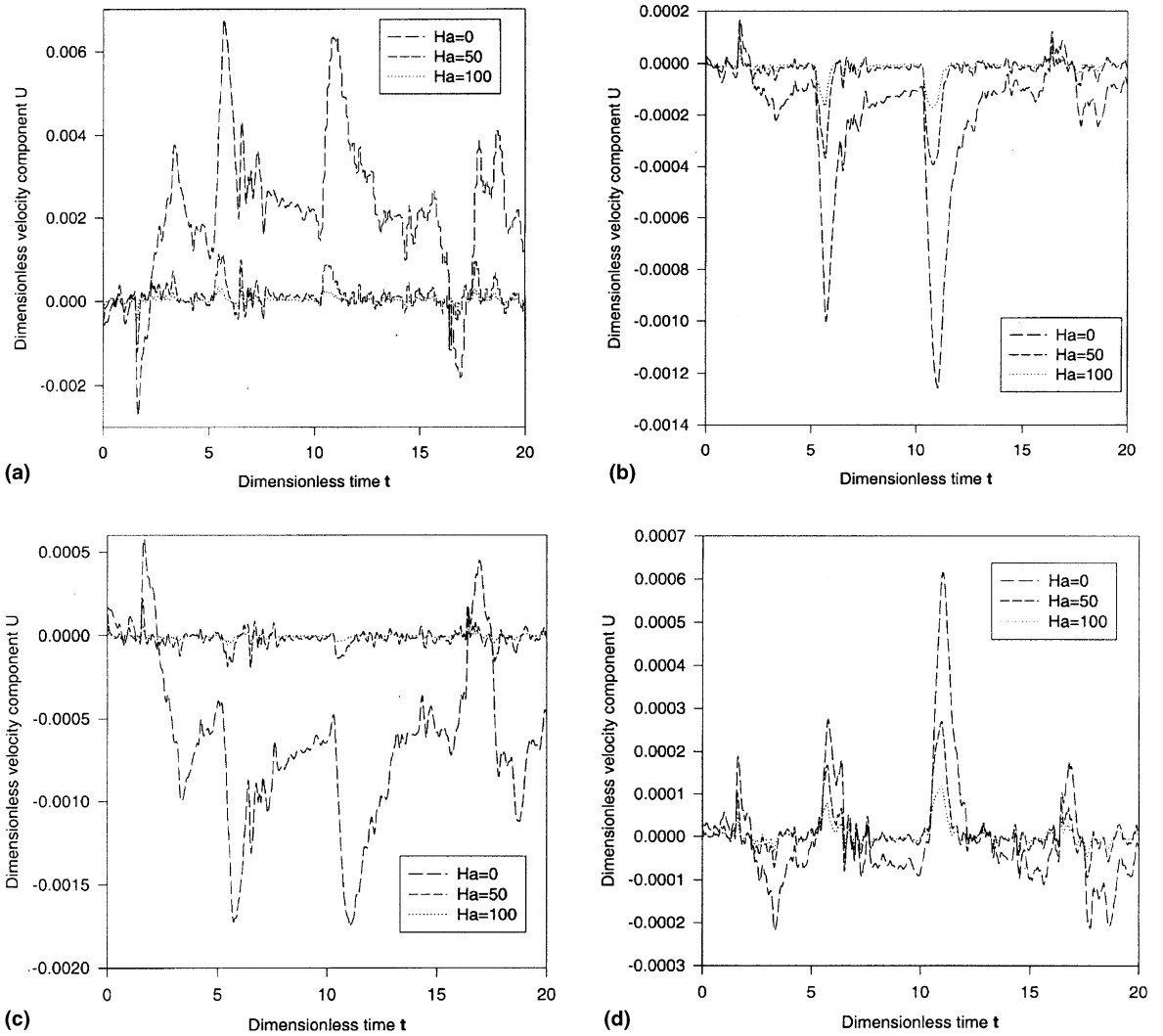

Fig. 11. Time variation of real g-jitter induced velocities at some points as a function of applied magnetic fields: (a) at point ($x = 0.5,\ y = 0.08$); (b) at point ($x = 0.08,\ y = 0.5$); (c) at point ($x = 0.5,\ y = 0.5$); and (d) at point ($x = 0.92,\ y = 0.5$).

system under consideration, the results show that the basic oscillating fluid flow and concentration patterns are very similar to those shown above. For a g-jitter component with frequency $= 0.001$ Hz, computed results duplicate those given in [4], further confirming the accuracy of our numerical computations. The results also indicate that the applied frequency can have a significant effect on both fluid flow intensity and concentration distribution. The flow intensity, $\mathbf{U}_{am}$, is found to be inversely related to the frequency of a g-jitter disturbance and increases with a decreasing frequency. This provides a confirmation on the same conclusions reached by analytical analyses [20]. The applied magnetic field is useful in damping the flows induced by the entire frequency range studied, and in particular, is more effective in damping out the lower frequency g-jitter induced flows.

While the idealized single frequency g-jitter force approximation is very valuable in helping to develop a fundamental understanding of the basic behavior of oscillating convective flows and concentration striation in the melt, it by no means can be used to fully represent real g-jitter perturbations. In fact, real g-jitter occurs randomly in direction, time and magnitude. Fig. 9 plots

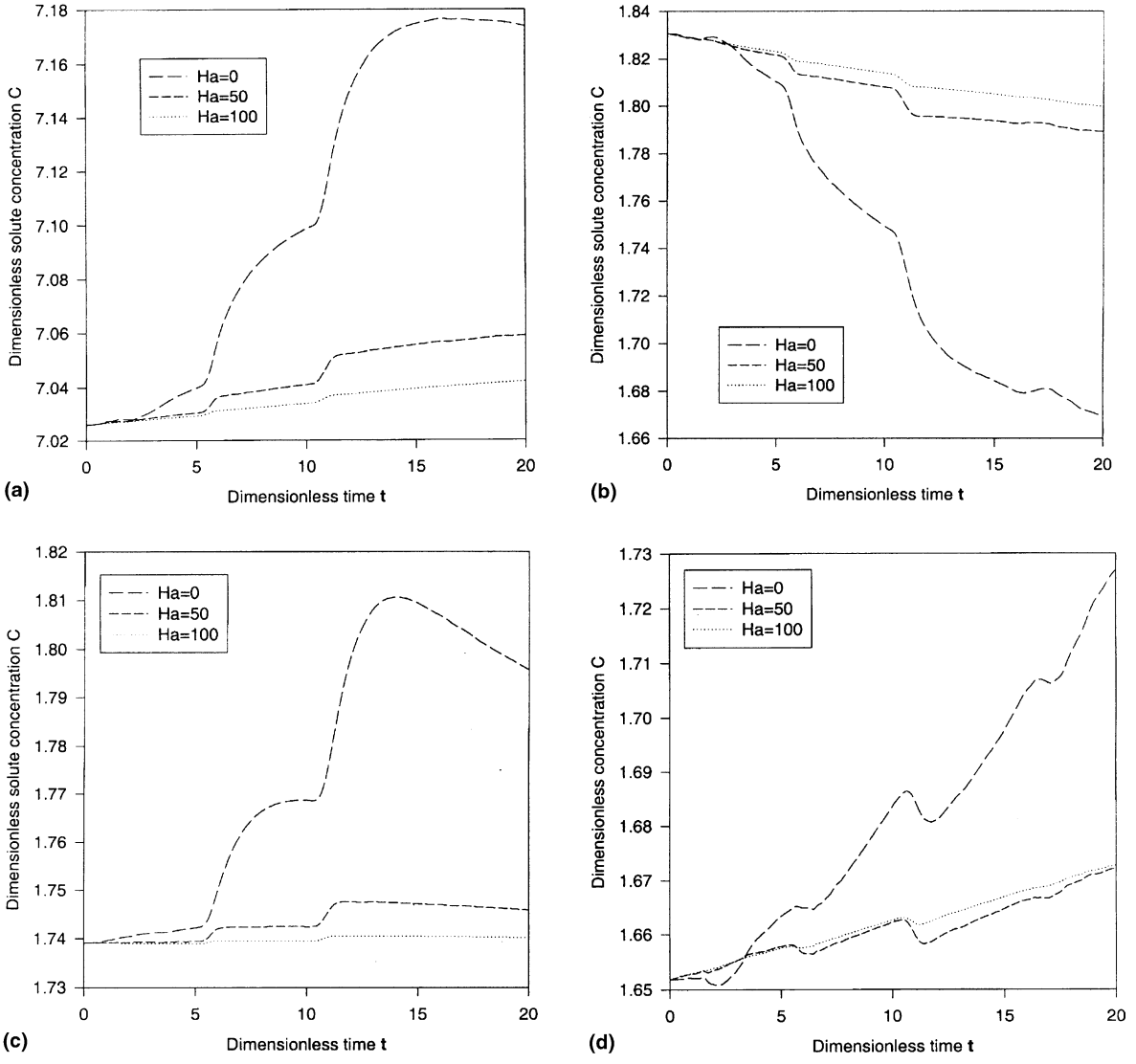

Fig. 12. Effect of magnetic fields on time variation of concentration at some points in the melt under the influence of real g-jitter: (a) at point ($x = 0.5,\ y = 0.08$); (b) at point ($x = 0.08,\ y = 0.5$); (c) at point ($x = 0.5,\ y = 0.5$); and (d) at point ($x = 0.92,\ y = 0.5$).

real g-jitter data measured during space flight. The velocity fields calculated using these real g-jitter data, with the initial field given in Fig. 3, are depicted in Fig. 10 with and without the presence of an applied magnetic field. The disturbance of the fluid flow field is apparent when the g-jitter takes effect. However, the perturbation is rather small and has a magnitude similar to the growth velocity for the present case in the absence of a magnetic field. This is in sharp contrast with the velocity field, which is almost uniform, when a magnetic field is applied (see Fig. 10(d)). The damping effect of a magnetic field on the g-jitter driven flows is further illustrated in Fig. 11, where the velocity fluctuations are plotted at different locations for the time period when the g-jitter is active. Apparently, the applied magnetic field causes a great reduction of flow velocity and is very effective in counterbalancing the effect of the g-jitter. The magnetic damping effect becomes even more pronounced for the spiking velocities that arise from the spikes of the g-jitter driving force. This provides a confirmation of the single frequency studies, which showed that the flow field induced by a higher g-jitter force is even more effectively reduced with an applied magnetic field.

The reduction of the velocity field leads to a more uniform solute distribution in the melt, as shown in

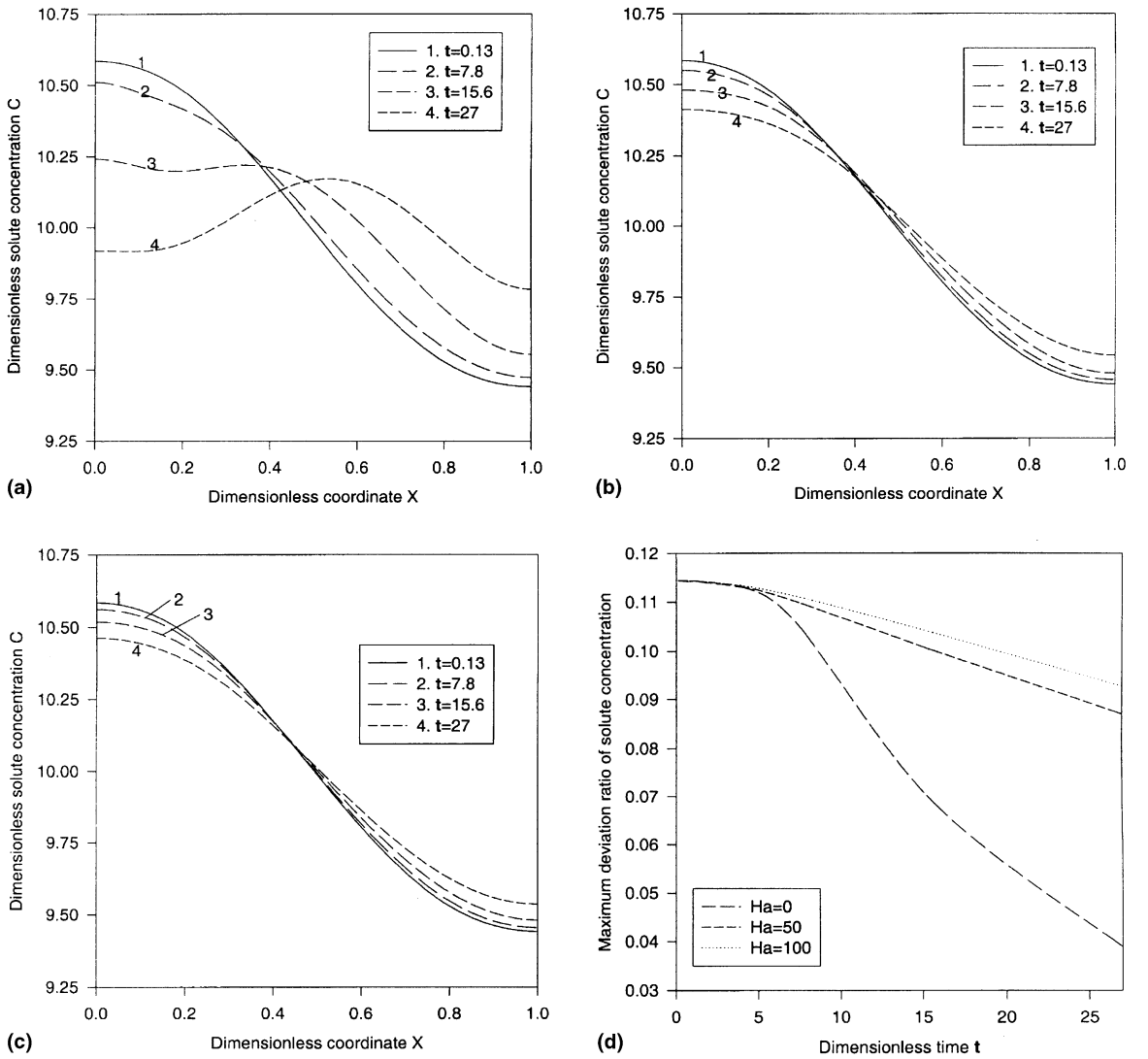

Fig. 13. Magnetic damping effects on the transient development of solute distribution along the solid–liquid interface ($Y = 0$) under the influence of real g-jitter: (a) $Ha = 0$, (b) $Ha = 50$, and (c) $Ha = 100$.

Fig. 12, where the time dependent concentration is plotted at several points for the period when the *g*-jitter is present. The solute striation along the lower solid–liquid interface (or solidification front) is also plotted in Fig. 13 at selected times after the real *g*-jitter sets in. Inspection of these results clearly suggests that a magnetic field is very effective in suppressing the time variation of concentration in the liquid pool.

The results discussed so far were obtained by applying the magnetic field at the onset of *g*-jitter disturbances. This should be an optimal choice from the standpoint of energy consumption. Another choice would be to leave the magnetic field on at all times during space flight. Numerical simulations were also conducted for both idealized and real *g*-jitter cases. The computed results of concentration striation along the solid–liquid interface are shown in Fig. 14 when the real *g*-jitter data were used. The calculations started with an initial flow, thermal and solution fields induced by a constant microgravity ($g(t) = 10^{-6}$g) oriented in the *x*-direction but with a magnetic field ($Ha = 50$)

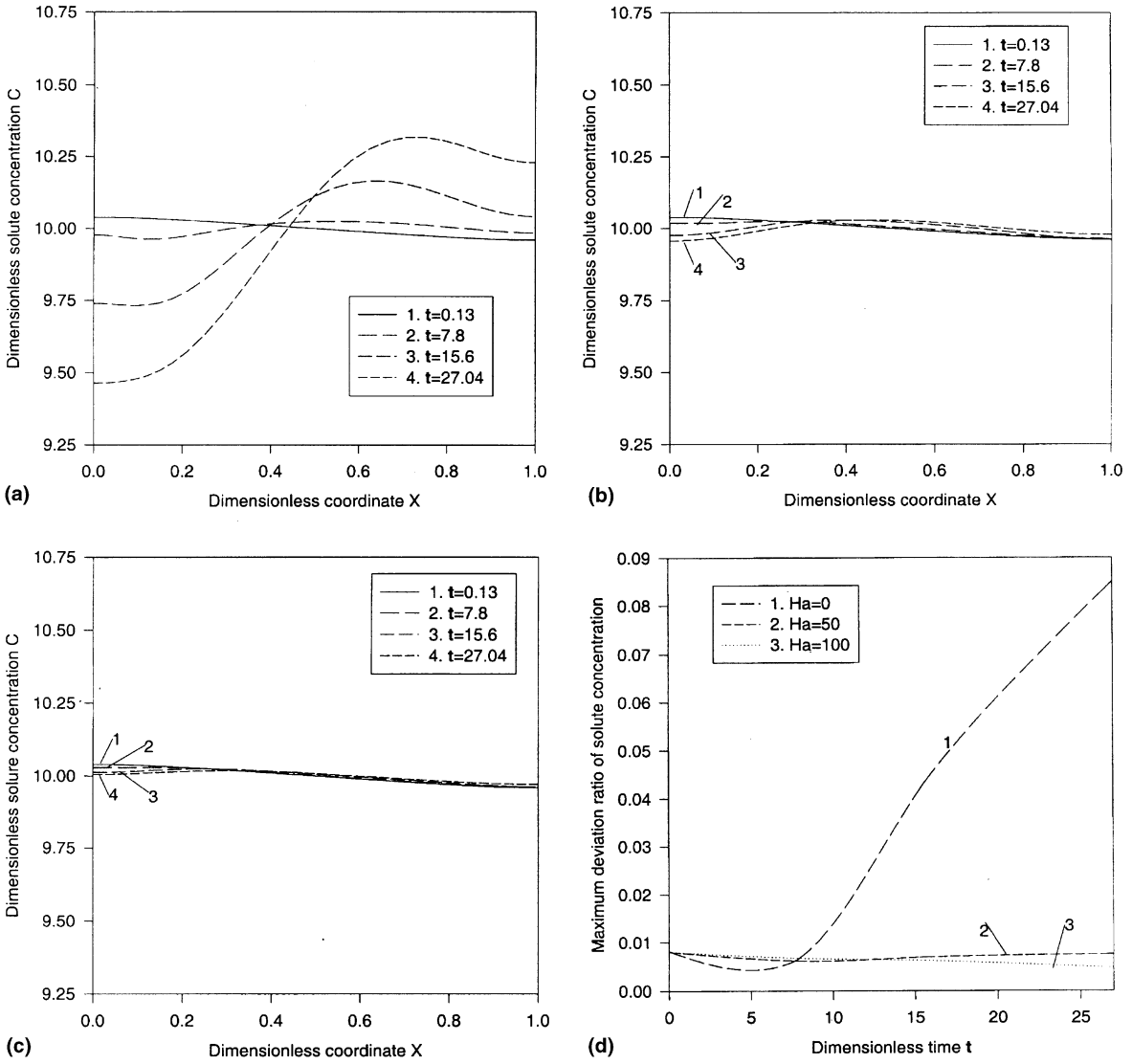

Fig. 14. Effect of initial conditions on the dynamic development of solute distribution along the solid–liquid interface ($Y = 0$) under the combined influence of real *g*-jitter and applied magnetic fields: (a) $Ha = 0$, (b) $Ha = 50$, and (c) $Ha = 100$. The initial conditions are calculated using the same parameters as in Fig. 2 but with an applied magnetic field ($Ha = 50$).

switched on prior to the onset of *g*-jitter. As a result, the initial flow field is much more quiescent. Comparison of these results with those in Fig. 13 indicates that the applied magnetic fields are very beneficial in suppressing the solutal striation and become more effective if they are switched on before the *g*-jitter disturbance sets in. Numerical simulations also showed that the same holds true for the idealized single frequency *g*-jitter.

5. Concluding remarks

This paper has presented a finite element model for the transient fluid flow, heat transfer and solute transport in the Bridgmann–Stockbarger single crystal growth processes. The numerical model development was based on the finite element solution of the fluid flow, energy and solute balance equations with an applied static magnetic field. The model was checked against available analytical solutions for some simplified geometry. Numerical simulations were carried out to study fluid flow, heat and mass transfer phenomena induced by the idealized single frequency and real *g*-jitter disturbances with and without an applied magnetic field. Computed results were presented to illustrate effects of various parameters on both the fluid flow and solute distributions in the melt pool. These results show that an applied magnetic field is very effective in suppressing unwanted *g*-jitter driven flow oscillation, thereby smoothing out solute striation in the liquid pool. It was found that flow induced by *g*-jitter follows the same oscillation frequency as the driving force with or without the applied field. However, with an applied magnetic field, the transient period after *g*-jitter sets in over which the flow field evolves to be quasi-steady state with time harmonic oscillation is reduced. The velocity intensity increases with an increase in *g*-jitter magnitude but decreases with an increase in the applied field strength. A time-varying concentration distribution results from *g*-jitter driven flows and this time variation is reduced with an applied magnetic field. The magnetic field is also very useful in suppressing the spiking velocities that result from the spikes in the real *g*-jitter data. The magnetic damping effects are more pronounced if the field is switched on before the occurrence of *g*-jitter disturbances.

Acknowledgements

The authors gratefully acknowledge the support of this work by NASA (Grant Nos.: NCC8-92 and NAG8-1693).

References

[1] H.C. De Groh III, E.S. Nelson, On residual acceleration during space experiments, in: ASME Winter Annual Meeting, HTD, vol. 290, Chicago, November 6–11, 1994, pp. 23–33.
[2] B.N. Antar, V.S. Nuotio-Antar, Fundamentals of low gravity fluid dynamics and heat transfer, CRC Press, Boca Raton, FL, 1993.
[3] S. Schneider, J. Straub, Influence of the Prandtl number on laminar natural convection in a cylinder caused by *g*-jitter, J. Cryst. Growth 97 (1989) 235–242.
[4] J.I.D. Alexander, S. Amiroudine, J. Quazzani, F. Rosenberger, Analysis of the flow gravity toleration of Bridgman–Stockbarger crystal growth I: steady state and impulse accelerations, J. Cryst. Growth 113 (1991) 21–38.
[5] J.I.D. Alexander, J. Quazzani, F. Rosenberger, Analysis of the flow gravity toleration of Bridgman–Stockbarger crystal growth II: transient and periodic accelerations, J. Cryst. Growth 97 (1989) 285–302.
[6] E.S. Nelson, An examination of anticipated *g*-jitter in space station and its effects on materials processes, NASA TM 10 3775, 1991.
[7] B.Q. Li, Stability of modulated-gravity-induced thermal convection in magnetic fields, Phys. Rev. E 63 (2001) 416–514.
[8] Y. Shu, B.Q. Li, H.C. de Groh, Numerical study of *g*-jitter induced double diffusive convection in microgravity, Numerical Heat Transfer B: Application 39 (3) (2001) 245–265.
[9] A.A. Wheeler, G.B. Mcfadden, B.T. Murray, S.R. Coriell, Convection stability in Rayleigh–Benard and directional solidification problems: high frequency gravity modulation, J. Phys. Fluids A 3 (1991) 2847–2853.
[10] J.I.D. Alexander, Low-gravity experiment sensitivity to residual acceleration: a review, Microgravity Sci. Tech. 2 (1994) 131–135.
[11] N. Ma, J.S. Walker, Magnetic damping of buoyant convection during semiconductor crystal growth in microgravity: spikes on residual acceleration, Phys. Fluids 8 (4) (1996) 944–949.
[12] J. Baumgartl, M. Gewald, R. Rupp, J. Stierlen and G. Muller, The use of magnetic fields and microgravity in melt growth of semiconductors: a comparative study, in: Proceedings of VIth European Symposium On Materials and Fluids Sciences in Microgravity, Oxford, UK, 1990, pp. 47–52.
[13] R.W. Series, T.J. Hurle, The use of magnetic fields in semiconductor crystal growth, J. Cryst. Growth 113 (1991) 305–345.
[14] H. Ben Hadid, D. Henry, R. Touihri, Unsteady three-dimensional buoyancy-driven convection in a circular cylindrical cavity and its damping by magnetic field, J. Cryst. Growth 180 (1997) 433–441.
[15] T. Alboussière, A.C. Neubrand, J.P. Garandet, R. Moreau, Segregation during horizontal Bridgman growth under an axial magnetic field, J. Cryst. Growth 181 (1997) 133–144.
[16] J. Baumgartl, G. Muller, The use of magnetic fields for damping the action of gravity fluctuations (*g*-jitter) during

crystal growth under microgravity, J. Cryst. Growth 169 (1996) 582–586.
[17] B. Pan, MS Thesis, Louisiana State University, 1997.
[18] S. Chandrasekhar, Hydrodynamic and Hydromagnetic Stability, Dover, New York, 1981.
[19] O.C. Zienkiewicz, R.L. Taylor, The Finite Element Method, fourth ed., McGraw-Hill, New York, NY, 1992.
[20] B. Pan, B.Q. Li, Effects of magnetic field on oscillating mixed convection, Int. J. Heat Mass Transfer 41 (1998) 2705–2710.